The Journal of Chemical Physics

Absorption-emission symmetry breaking and the different origins of vibrational structures of the ^1Q_y and ^1Q_x electronic transitions of pheophytin *a*

Cite as: J. Chem. Phys. **151**, 165102 (2019); https://doi.org/10.1063/1.5116265
Submitted: 24 June 2019 . Accepted: 29 September 2019 . Published Online: 30 October 2019

Margus Rätsep, Juha Matti Linnanto, Renata Muru, Malgorzata Biczysko, Jeffrey R. Reimers, and Arvi Freiberg

The Journal of Chemical Physics ARTICLE scitation.org/journal/jcp

Absorption-emission symmetry breaking and the different origins of vibrational structures of the ^1Q_y and ^1Q_x electronic transitions of pheophytin *a*

Cite as: J. Chem. Phys. 151, 165102 (2019); doi: 10.1063/1.5116265
Submitted: 24 June 2019 • Accepted: 29 September 2019 •
Published Online: 30 October 2019

Margus Rätsep,[1,a] Juha Matti Linnanto,[1,b] Renata Muru,[1,c] Malgorzata Biczysko,[2,d] Jeffrey R. Reimers,[2,3,e] and Arvi Freiberg[4,f]

AFFILIATIONS

[1]Institute of Physics, University of Tartu, W. Ostwaldi 1, 50411 Tartu, Estonia
[2]International Centre for Quantum and Molecular Structures and Department of Physics, Shanghai University, Shanghai 200444, China
[3]School of Mathematical and Physical Sciences, University of Technology Sydney, Sydney, NSW 2007, Australia
[4]Institute of Physics, University of Tartu, W. Ostwaldi 1, 50411 Tartu, Estonia and Institute of Molecular and Cell Biology, University of Tartu, Riia 23, 51010 Tartu, Estonia

[a]**Electronic mail:** margus.ratsep@ut.ee
[b]**Electronic mail:** juha.matti.linnanto@ut.ee
[c]**Electronic mail:** renata.muru@gmail.com
[d]**Electronic mail:** biczysko@shu.edu.cn
[e]**Electronic mail:** jeffrey.reimers@uts.edu.au
[f]**Electronic mail:** arvi.freiberg@ut.ee

ABSTRACT

The vibrational structure of the optical absorption and fluorescence spectra of the two lowest-energy singlet electronic states (Q_y and Q_x) of pheophytin *a* were carefully studied by combining low-resolution and high-resolution spectroscopy with quantum chemical analysis and spectral modeling. Large asymmetry was revealed between the vibrational structures of the Q_y absorption and fluorescence spectra, integrally characterized by the total Huang-Rhys factor and reorganization energy in absorption of $S^A_{vib} = 0.43 \pm 0.06$, $\lambda^A = 395\ cm^{-1}$ and in emission of $S^E_{vib} = 0.35 \pm 0.06$, $\lambda^E = 317\ cm^{-1}$. Time-dependent density-functional theory using the CAM-B3LYP, ωB97XD, and MN15 functionals could predict and interpret this asymmetry, with the exception of one vibrational mode per model, which was badly misrepresented in predicted absorption spectra; for CAM-B3LYP and ωB97XD, this mode was a Kekulé-type mode depicting aromaticity. Other computational methods were also considered but performed very poorly. The Q_x absorption spectrum is broad and could not be interpreted in terms of a single set of Huang-Rhys factors depicting Franck-Condon allowed absorption, with Herzberg-Teller contributions to the intensity being critical. For it, CAM-B3LYP calculations predict that S^A_{vib} (for modes >100 cm^{-1}) = 0.87 and $\lambda^A = 780\ cm^{-1}$, with effective *x* and *y* polarized Herzberg-Teller reorganization energies of 460 cm^{-1} and 210 cm^{-1}, respectively, delivering 15% *y*-polarized intensity. However, no method was found to quantitatively determine the observed *y*-polarized contribution, with contributions of up to 50% being feasible.

I. INTRODUCTION

Pheophytin *a* (Pheo-a), a chlorophyll derivative deprived of its central Mg^{2+} ion (Fig. 1), is the first electron carrier intermediate in the reaction center of photosystem II, thus playing an important role in photosynthesis.[1] Despite this, its photophysical properties, which are distinct from chlorophyll *a* (Chl-a), as demonstrated in Refs. 2–4, have not been fully characterized, including its ^1Q_y

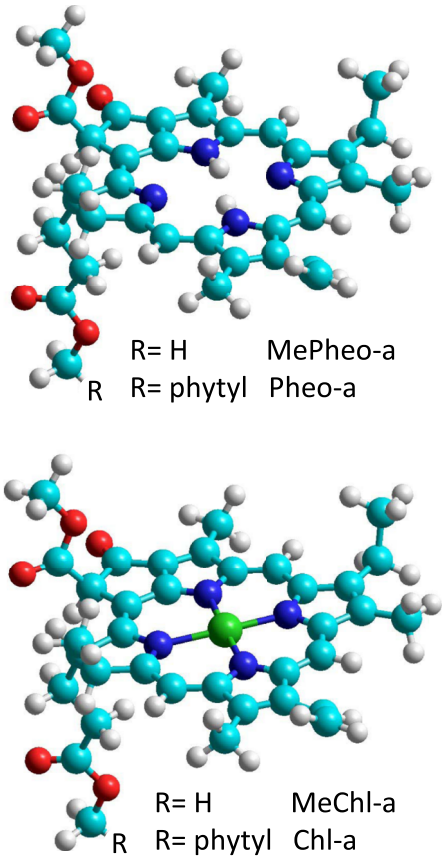

FIG. 1. CAM-B3LYP/6-31G* optimized structures of MePheo-a and MeChl-a. C—cyan, N—blue, O—red, H—white, Mg—green.

high-resolution emission spectrum, ^1Q_y absorption/emission asymmetry, and the nature of its ^1Q_x absorption spectrum.

The classical four-orbital Gouterman model[5] describes the critical spectroscopic features of porphyrins, chlorophylls, pheophytins, etc., in terms of two independent low-energy Q-band electronic transitions, named Q_y and Q_x, and two analogous independent high-energy Soret-band electronic transitions, named B_x and B_y; the transition components are named after their polarization directions within the macrocycle plane. Although early magnetic circular dichroism[6] (MCD) and high resolution fluorescence-excitation[7] measurements corroborated the model for Pheo-a, it was questioned later based on linear dichroism experiments[8] and density functional theory (DFT) calculations,[9] with results being interpreted in terms of additional bands interfering with the Q bands. However, the excited states of Chl-a and Pheo-a were then studied using SAC-CI[10] and multireference DFT,[11] supporting the original Gouterman model.

Recently, a new assignment for Chl-a was introduced that accounts for all observed data by abandoning the classical idea that Q_x and Q_y form independent bands, instead being intricately mixed by resonant vibronic coupling.[2] A consequence of this is that the spectral profiles of the Q bands cannot be described using the standard Franck-Condon (FC) approximation[12] in terms of only Huang-Rhys factors.[13] In addition, transition intensity arises from the Herzberg-Teller (HT) mechanism,[14–16] in this case depicting extremely strong nonadiabatic coupling between the Q_x and Q_y states.[17–23] Using this ansatz, a qualitative understanding of the Q-band spectra of 32 chlorophylls and their derivatives in different solvent combinations was established, including Pheo-a, assuming that the four-orbital model is generally valid, whereas the Born-Oppenheimer approximation[24–27] fails. As Pheo-a contains no metal centers that could introduce unwanted complications in quantum chemical analysis and spectral modeling, and as for it pure samples and high-resolution spectra can be obtained, detailed quantitative understanding of the spectroscopy of its Q_x and Q_y states is feasible, providing a significant test for the reliability of the new assignment.

In this work, the detailed structure of optical absorption and fluorescence spectra related to the Q_y and Q_x singlet electronic states of Pheo-a were studied by combined experimental and quantum chemical analyses, as well as by spectral simulation methods. In addition to the accurate measurement of low-resolution Q-band absorption and emission spectra, our experimental research focused on measuring high-resolution Q_y absorption and fluorescence emission spectra in a frozen glassy matrix at liquid-He temperatures. The homogeneous fluorescence spectra were obtained using the highly selective difference fluorescence-line-narrowing (ΔFLN) spectroscopy, which combines both spectral hole-burning and FLN techniques.[28–31] All experimental results were then analyzed and modeled by quantum chemistry methods, seeking consistency with the core predictions of the four-orbital spectroscopic model. The Q_y band is found to be very well described using just Huang-Rhys factors to represent the influence of vibrational motions, as previously suggested.[2,32] Large asymmetry is observed between the absorption and emission spectra of Q_y, an effect interpreted in terms of Duschinsky rotation[33] of the normal modes of vibration between S_0 and Q_y. Alternatively, the Q_x transition is found to be strongly influenced by the Herzberg-Teller intensity.

II. MATERIALS AND METHODS

A. Sample

Pheo-a was prepared from leafs of sunflower (*Helianthus annuus*) by treatment of the extract with a small volume of 0.75 mM HCl as described earlier by Eijckelhoff and Dekker,[34] followed by thin-layer chromatography. Further purification was performed by high performance liquid chromatograph HPLC 20A Prominence (Shimadzu) at 30 °C. The used solvent (methanol/ethyl acethate with 4:1 volume ratio) was subsequently removed under vacuum at room temperature. This resulted in a highly pure sample, as established in supplementary material, Sec. S1. The powder of Pheo-a was stored in dark at 4 °C. Commercially available high-grade triethylamine (TEA) was used as solvent in optical measurements. At low temperatures, plastic (PMMA) cuvettes of 10 mm path length and gelatine capsules of 4 mm diameter were used as sample containers for absorption and fluorescence experiments, respectively.

B. Spectroscopy

Selective excitation of fluorescence was performed using a model 375 dye laser of 0.5 cm^{-1} linewidth pumped by a Millennia Prime solid state laser (both Spectra Physics, USA). Nonselective fluorescence was excited by a 5 mW diode laser at 407 nm. For transmission measurements, a high-stability tungsten light source BPS100 (BWTek, USA) was employed. All the spectra were recorded with a 0.3-m spectrograph Shamrock SR-303i equipped with a thermo-electrically cooled CCD camera DV420A-OE (both Andor Technology, UK). The fluorescence spectra were corrected for the wavelength sensitivity of the detection system. Low-temperature measurements were performed at 4.5 ± 0.2 K using a He bath cryostat (Utreks, Ukraine). The temperature was measured with a calibrated silicon diode and a temperature monitor model 211 (Lakeshore Cryotronics, USA).

C. Data analysis

The experimental absorption and fluorescence spectra were preliminarily analyzed in terms of dimensionless Franck-Condon-allowed[12] electron-phonon and electron-vibration interactions represented by Huang-Rhys factors.[35] These factors have simple physical meanings, being the mean number of phonons/vibrations excited when the electronic state is changed at fixed nuclear geometry in a way that is geometry independent. However, this analysis ignores the possibility that the transition moment could change during the zero-point motion about the initial nuclear geometry, a non-Condon effect. If the transition moment is taken to be linearly proportional to initial-state geometry changes from equilibrium, the Herzberg-Teller effect is generated (see below).[14] Also, by considering explicitly only intensity-derived Huang-Rhys factors, all analyses assume that the potential-energy surfaces are harmonic and that the final states differ from the initial ones only by coordinate shifts. In this way, more elaborate properties such as the Duschinsky rotation matrices[33] that correlate the normal modes of the initial and final states are not required to be specified. Hence, the effects of Duschinsky rotation other than the differentiation of absorption and emission Huang-Rhys factors, as well as associated possible force-constant changes, are neglected.

This approach allows the linear electron-phonon coupling strength, commonly described as the Huang–Rhys factor S_{ph}, to be evaluated directly from the experimental spectra as

$$\exp(-S_{ph}) = \frac{I_{ZPL}}{I_{ZPL} + I_{PSB}}. \tag{1}$$

In Eq. (1), I_{ZPL} and I_{PSB} are the integral intensities of the 0–0 zero-phonon line (ZPL) and the phonon sideband (PSB), respectively. The relative intensity of a sideband to the ZPL is also often represented using the Debye–Waller factor, $\alpha = \exp(-S_{ph})$.

The Franck-Condon allowed vibrational coupling strength, S_j, for a discrete (jth), intramolecular vibrational mode was calculated as

$$S_j = \frac{I_j}{I_{ZPL} + I_{PSB}}, \tag{2}$$

where I_j is the integral intensity of the line attributable to a 0–1 Franck-Condon-allowed transition. Accordingly, the total vibrational coupling strength, S_{vib}, is obtained as

$$S_{vib} = \frac{I_{vib}}{I_{ZPL} + I_{PSB}}, \tag{3}$$

where I_{vib} is the intensity of the band corresponding to all 0–1 transitions. In the case of $S_j \ll 1$, the total Huang-Rhys factor can approximately be obtained as $S_{vib} \approx \sum_j S_j$.

The Franck-Condon effects can also be characterized in terms of the associated optical reorganization energies,

$$\lambda_j = h\nu_j S_j, \tag{4}$$

and the total reorganization energy $\lambda = \sum_j \lambda_j$ that quantifies the amount of energy released when a vertically excited molecule relaxes to its vibrational ground state. The total reorganization energy can be readily determined from low-resolution spectra as the difference between the average transition energy and the energy of the 0–0 band origin, e.g., for absorption A,

$$\lambda = \frac{h\int_0^\infty A(\nu)d\nu}{\int_0^\infty \nu^{-1}A(\nu)d\nu} - h\nu_{0-0}. \tag{5}$$

It can also be calculated directly by electronic-structure computational techniques as the energy difference between the vertically and adiabatically excited geometries, not requiring the evaluation of actual band shapes,

$$\lambda = E^F(\mathbf{Q}^I) - E^F(\mathbf{Q}^F), \tag{6}$$

where E^F is the energy of the final state, evaluated here both at the equilibrium geometries of the final state ($\mathbf{Q}^F$) and the initial state ($\mathbf{Q}^I$).

In some spectral modeling, both Franck-Condon and Herzberg-Teller effects were included. The Franck-Condon approximation assumes that the electronic transition moment $\mathbf{M}$ is a constant, independent of nuclear geometry, taking on its value $\mathbf{M}_0$ at the ground-state equilibrium geometry $\mathbf{Q}^I$, while Herzberg-Teller effects arise, assuming that it changes from this value in proportion to nuclear displacement according to Refs. 14, 20–22, 36, and 37,

$$\mathbf{M} = \mathbf{M}_0 + \sum_j \mathbf{m}_j Q_j, \quad \mathbf{m}_i = \frac{d\mathbf{M}}{dQ_j}, \tag{7}$$

where the dimensionless normal coordinate Q_j measures, in terms of the zero-point motion, the extent of vibrational displacement $\mathbf{Q}^F$ in each of the final-state normal coordinates. Each Herzberg-Teller active vibration produces a vibronic origin at the energy of the real origin plus the vibrational contribution $h\nu_j$, with an intensity relative to that of the usual Franck-Condon origin of $|\mathbf{m}_j|^2/2|\mathbf{M}_0|^2$. Each vibronic origin therefore contributes to the total intensity in a way describable by an effective reorganization energy

$$\lambda_j^{HT} = h\nu_j|\mathbf{m}_j^2|/2|\mathbf{M}_0|^2. \tag{8}$$

Upon each vibronic origin, an entire Franck-Condon progression is then built, describable by the same Huang-Rhys factors

obtained using Eq. (2) applied to the actual band origin. This gives the spectral illusion that multiple electronic transitions (e.g., non-Gouterman bands) are involved, whereas in reality there is only one excited electronic state. The Herzberg-Teller intensity is usually described as being *borrowed* from some nearby Franck-Condon allowed electronic state(s). The Huang-Rhys factors are themselves evaluated from the computed data by an analogous procedure, noting that

$$S_j = \frac{\delta_j^2}{2}, \tag{9}$$

where δ_j is the change in the geometry between the two states involved in the transition projected onto the dimensionless normal coordinates Q_j.

D. Quantum chemical and spectral modeling

The Franck-Condon electronic absorption and emission spectra of methyl pheophorbide *a* (MePheo-a), Fig. 1, were simulated by optimizing the geometry of the ground, Q_y, and Q_x states using either Gaussian-16[38] or MOPAC,[39] followed by normal-mode analyses, evaluation of the projections of the resulting geometry changes onto these normal modes using curvilinear coordinate[40] analysis,[41] and then spectral simulation at 0 K using the DUSHIN program.[41] All transitions were included containing up to six vibrational quanta in each mode. Other approximations used in this analysis are as follows: neglect of the anharmonic kinetic-energy terms associated with curvilinear coordinates, neglect of anharmonic contributions beyond the often critical ones represented through use of curvilinear coordinates, use of an approximate orthogonalization of the Duschinsky matrix, and neglect of contributions from the Duschinsky matrix that redistribute intensity amongst transitions involving multiple-mode excitations; these approximations all have effects of similar magnitude and mostly influence spectral tails and other details at high resolution.[42] The critical effect of the Duschinsky matrix on differentiating absorption and emission Huang-Rhys factors is fully included, and subtler effects modifying relative intensities of spectral progressions is also included. All low-frequency modes are included, even though these are poorly represented as the calculations are performed in the absence of explicit atoms representing the surrounding environment. They are wise to neglect[43] but are included here as, in this case, they appear to have no deleterious effect on spectra calculated using the above assumptions.

The electronic-structure methods used to calculate the structure and normal modes included time-dependent DFT (TDDFT) approaches utilizing the range-corrected hybrid functionals CAM-B3LYP,[44,45] ωB97XD,[46] and LC-ωHPBE;[47] the hybrid functionals B3LYP,[48] PBE0,[49] HSE06,[50] and MN15;[51] and the generalized-gradient-approximation density functional PBE.[52] In addition, the semiempirical method PM6[53] (using 3 occupied and 3 unoccupied orbitals in the configuration interaction), and the Hartree-Fock (HF)[54] and configuration-action singles (CIS)[55] methods, was used. Except for some test calculations using larger basis sets, the 6-31G*[56] basis was used throughout. A Gaussian random homogeneous distribution of transition energies was applied to smooth the calculated spectra with a standard deviation σ (resolution 2σ) that was medium and state dependent. As the Q_y and Q_x transition-moment directions are not exactly orthogonal to each other, *x* and *y* directions were chosen to minimize the differences between them and the orthogonal-vector set used in the calculations.

The transition moment derivatives $\mathbf{m}_j$ were evaluated by numerical differentiation.[20–23] The appearance of the Herzberg-Teller intensity is a fundamental indicator of the failure of the Born-Oppenheimer approximation, demanding in general the full solution of nonadiabatic coupling equations in order to obtain spectra.[17–23] Indeed, this step is essential for understanding the spectra of Chl-a as for it the Q_x and Q_y states come into resonance.[2] However, for Pheo-a, the large Q_x-Q_y energy gap, which is yet small enough to support large B_x-Q_x and large B_y-Q_x energy gaps, allows perturbation theory to be used to construct spectra using simple adiabatic approaches, as implemented in the DUSHIN suite,[20–23,41] although much more computationally expensive non-perturbative approaches are also available therein. For porphyrin, a related molecule in which the Q_x state is lower in energy than Q_y, the perturbative approach has been shown to be appropriate only for simulation of the emission spectrum.[57] Simulation of the Pheo-a Q_x absorption spectrum presents a somewhat analogous situation as the vibronic levels of interest are far removed from the origins of other states in each case, making appropriate the use of the Born-Oppenheimer approximation to calculate spectra.

III. EXPERIMENTAL RESULTS

A. Low resolution absorption and fluorescence spectra of Pheo-a

Figure 2 shows the conventional low-resolution absorption spectrum of Pheo-a in TEA at 290 K (drawn in blue) over the visible range of the optical spectrum measured at ambient temperature. The major spectral lines indicated belong to different singlet electronic

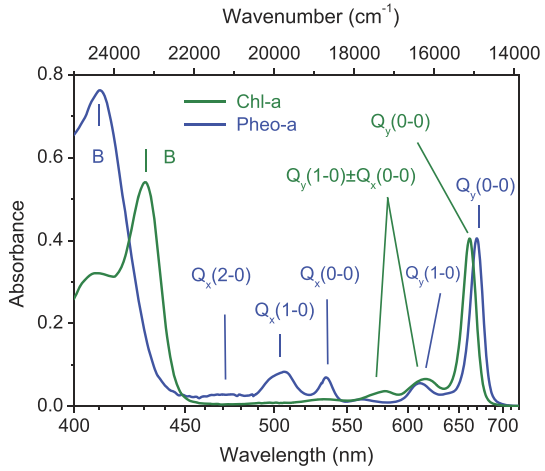

FIG. 2. Absorption spectra of Pheo-a (blue) and Chl-a (green) both in TEA at ambient temperature (290 K and 295 K, respectively). The two spectra presented in reciprocal wavelength scale (linear in energy) are normalized by the Q_y transition peak intensity. Interpretation of different spectral structures indicated by vertical lines is also shown.

transitions in individual Pheo-a molecules. A similar spectrum for Chl-a is also shown in the figure for reference (green).

As shown in Fig. 1, in comparison with Chl-a, the porphyrin ring of Pheo-a is deprived of a central Mg^{2+} ion, being replaced by two protons (H^+). The indicated relatively minor change in spatial structure causes significant modification of the pigment electronic structure that is reflected in its transformed absorption spectrum (Fig. 2). While the low-resolution $Q_y(0–0)$ band-origin positions for Pheo-a and Chl-a are quite similar, great differences are evident in the rest of the spectra. Most remarkably, the Q-band manifold of Pheo-a well separates into two individual transitions with the Q_y origin $Q_y(0–0)$ at 669 nm and $Q_x(0–0)$ at 535 nm. This is drastically different from Chl-a, where, as recently revealed,[2] the $Q_x(0–0)$ transition is strongly perturbed by resonant vibronic coupling with part of the $Q_y(1–0)$ vibrational sideband (~610 nm) and gets split into two components found around ~580 nm (strong) and ~630 nm (weak). The Soret band of Chl-a peaks at 430 nm, whereas in Pheo-a it is shifted toward the shorter wavelength of 411 nm.

Figure 3 shows absorption and fluorescence spectra of Pheo-a in frozen TEA glass at 4.5 K. At such low temperatures, inhomogeneous broadening is reduced, making the vibrational structures more evident. The three maxima appearing at 637, 611, and 561 nm represent vibrational structure coming from Q_y absorption. The analogous structure associated with the Q_x transition is seen at 511, 502, and 475 nm. The relatively weak absorption bands at 561 and 475 nm have been assigned to the vibrational overtones $Q_y(2–0)$ and $Q_x(2–0)$, whereas the other transitions are resolved components of $Q_y(1–0)$ or $Q_x(1–0)$. Sample purity, and the attribution of these spectral features to isolated monomers rather than aggregates, is discussed in supplementary material, Sec. S1.

Like in the case of Chl-a and bacteriochlorophyll-a,[4,43] the Q_y absorption and fluorescence spectra of Pheo-a lack mirror symmetry. This is highlighted in Fig. 4(a) where the absorption band strength (A/ν) at 4.5 K in TEA, presented as $\Delta\nu$ relative to its origin, is compared to the emission band strength (E/ν^3 or E/ν^5 if spectra were measured sweeping linear in wavelength) reflected about its origin. The vibrations most active in absorption have almost 500 cm^{-1} higher frequency than in fluorescence. Worth also noticing is a spectrally broader Q_x origin line compared with

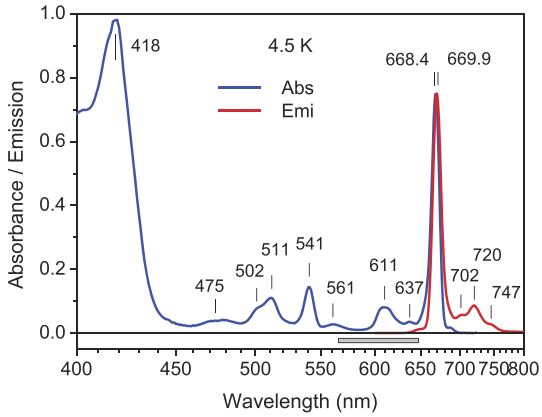

FIG. 3. The Q_y peak normalized absorption (blue) and fluorescence (red) spectra of Pheo-a in TEA glass at 4.5 K. The fluorescence was excited nonresonantly into the Soret absorption band at 407 nm. Numbers indicate spectral wavelengths in nanometers. The horizontal bar defines the excitation range (565–650 nm) applied in measurements of high-resolution fluorescence excitation spectra shown in Fig. 5. Please notice the reciprocal wavelength scale applied.

that of Q_y, also observed for bacteriochlorophyll-a.[43] In Ref. 43, this was explained by the shorter lifetime of the Q_x state and the resulting greater homogeneous broadening of the absorption line.

Deviating from each other appear as well the vibrational sidebands of the Q_y and Q_x electronic transitions [Figs. 3 and 4(b)]. The Q_x origin at 541 nm has a relatively very strong and broad first-order vibrational sideband shifted by ~1060 cm^{-1} away from it toward higher energy and a shoulder at ~1440 cm^{-1}. In the sideband of the Q_y transition, only latter distribution of frequencies is recognizable. Assuming that all of the sideband absorption occurs through Franck-Condon allowed processes, the total Huang-Rhys factor related to the Q_y absorption is determined using Eq. (3) as $S^A_{vib}(Q_y) = 0.43 \pm 0.06$ and that of the Q_x transition $S^A_{vib}(Q_x) \sim 1.6$. This is different from bacteriochlorophyll-a, another molecule for which the two Q bands are well-separated from each other, where

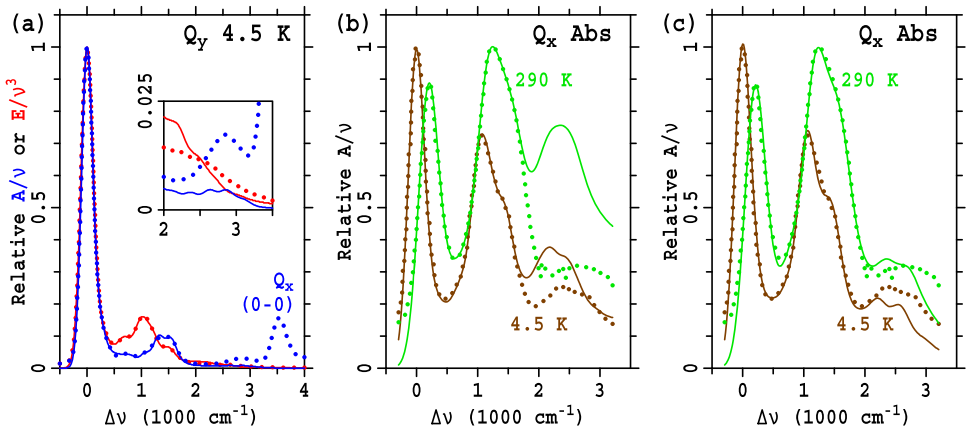

FIG. 4. Fitting of experimental low-resolution spectra of Pheo-a (points) to models (solid lines) involving a minimal number of Franck-Condon displaced modes [(a) and (b)], and this plus a minimum number of independent Herzberg-Teller active modes (c), see Tables I and II and Table S1. Shown in (a) are the Q_y absorption (blue) and reflected emission (red) spectra at 4.5 K in TEA glass (Fig. 3), and shown in (b) and (c) are the Q_x absorption spectra at 290 K in TEA solution (Fig. 2). All the spectra are presented relative to their appropriate origin.

relative intensities of vibrational contributions to the Q_y and Q_x origin transitions appear roughly equal.[43]

The assumption of only Franck-Condon allowed intensity is tested for Q_y in Fig. 4(a) where the vibrational sidebands are modeled using a minimalist approach, assuming 7 displaced modes. The absorption and emission spectra are mostly accurately fitted, with resulting vibrational frequencies, Huang-Rhys factors, and derived reorganization energies listed in Table I. From the absorption fit, the total $S^A_{vib}(Q_y) = 0.43$, in good agreement with the estimate based on Eq. (3); the associated total reorganization energy is $\lambda^A = 355\ cm^{-1}$. From the emission fit, $S^E_{vib}(Q_y) = 0.49$ and $\lambda^E = 402\ cm^{-1}$.

Some deviation between the fitted and observed absorption spectra is found in Fig. 4(a) (highlighted in the inset) in the region of $\Delta\nu = 2800\ cm^{-1}$ from $Q_y(0–0)$ (~561 nm), the region of the (2–0) vibrational sideband, see Fig. 3. No analogous deviation is found for the emission spectrum. This indicates that absorption arising from some process other than Franck-Condon allowed Q_y excitation is occurring. One possibility is that this absorption is associated with some non-Gouterman state,[8,9] and another is that it ascends through the Herzberg-Teller mechanism, owing to near-resonant vibronic coupling of $Q_y(2–0)$ to the nearby $Q_x(0–0)$ band.

These two possibilities can, in principle, be distinguished by selective excitation of fluorescence into the 561-nm band, as reported in Fig. 5(b). At wavelengths shorter than 599 nm, the fluorescence signal gets weaker and loses structure in accordance with decreasing absorption. Nevertheless, when the laser wavelength approaches the 561-nm band, the structured fluorescence within the inhomogeneous distribution function (IDF) wavelengths once again appears. Although the lines around 2604–2872 cm^{-1} are rather broad and not very well resolved, the emerging structure supports the assignment of the 561-nm band as the (2–0) vibrational sideband of the Q_y state, in accord with the traditional Houssier and Sauer[6] tagging. Its anomalous intensity must therefore arise through vibronic coupling to $Q_x(0–0)$.

TABLE I. Fitting[a] of the low-resolution spectra of Q_y Pheo-a in TEA at 4.5 K in terms of a minimalist model containing 7 Franck-Condon-active vibrational modes; see Fig. 4(a).

Ground state vibrations (emission)			Q_y vibrations (absorption)		
$\nu\ (cm^{-1})$	S	$\lambda\ (cm^{-1})$	$\nu\ (cm^{-1})$	S	$\lambda\ (cm^{-1})$
1500	0.042	63	1550	0.072	112
1200	0.080	96	1320	0.088	116
1000	0.125	125	1070	0.039	42
800	0.039	31	800	0.031	25
650	0.068	44	600	0.029	17
420	0.045	19	400	0.031	13
250	0.092	23	220	0.135	30
Total	0.492	402	Total	0.426	355

[a]Using inhomogeneous broadening σ of 110 cm^{-1} for emission and 100 cm^{-1} for absorption.

Yet the absorption of Q_x could not be fitted at all on the assumption of just Franck-Condon intensity, as shown in Fig. 4(b). This indicates that a significant fraction of the Q_x intensity arises from vibronic coupling involving Q_x and some other state, most likely one or more of Q_y, B_x, and B_y. If the coupled state is B_x, then the Herzberg-Teller intensity will be *x* polarized, akin to the Franck-Condon allowed intensity. Furthermore, if the same vibrational modes attract both types of intensity, then the two sources can constructively or destructively interfere with each other, making for very uniquely shaped spectra. In general, this would not be expected to be the case as the chemical processes driving the two mechanisms are fundamentally different, and indeed, in supplementary material, Sec. S3, CAM-B3LYP calculations predict minimal correlation (also shown therein, the displaced modes of Q_x are uncorrelated to those

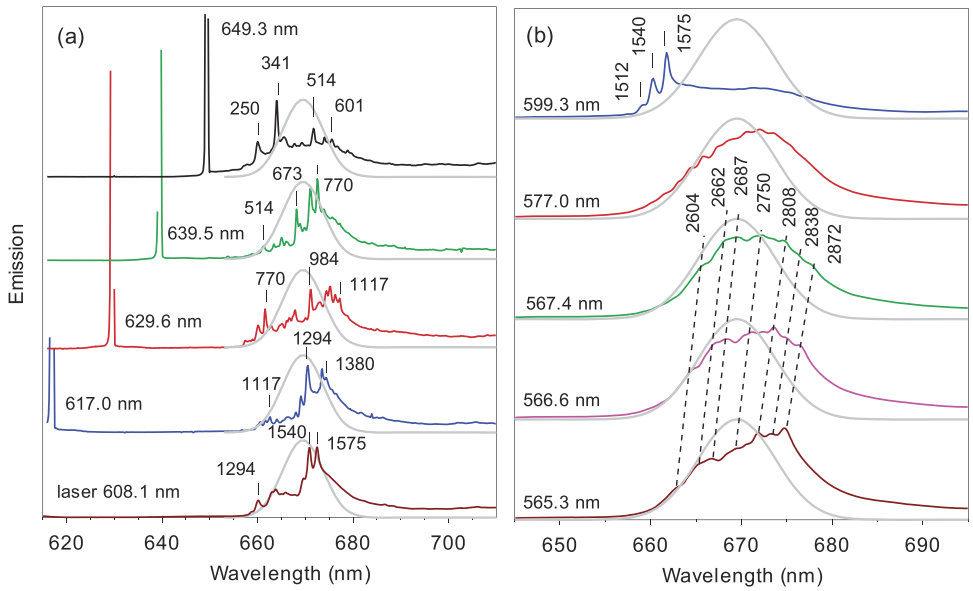

FIG. 5. Selectively excited fluorescence spectra of Pheo-a Q_y in TEA at 4.5 K. The spectra excited at different wavelengths indicated within the Q_y vibronic absorption band (the range highlighted in Fig. 3) are for clarity vertically shifted with respect to each other. The Gaussian IDF corresponding to 0–0 transitions is drawn by a gray line. Numbers without units designate vibrational frequencies in wavenumbers. Note different excitation and recording wavelength scales applied in parts (a) and (b).

for Q_y). If all modes are different, then no interference can occur and the spectrum will just be the sum of the intensities coming from both sources. Most significantly, the bandshape will then not contain information telling if the Herzberg-Teller polarization is in the *x* or *y* directions. Assuming only the Franck-Condon intensity, fitting spectra suggest that $S^A_{vib}(Q_x)$ = 1.57 at 4.5 K and 2.03 at 290 K [Fig. 4(b), Table II, supplementary material Table S1]. Such profound changes with temperature are, however, indicative of Herzberg-Teller mechanisms. Assuming that the Franck-Condon allowed intensity is temperature independent, both absorption spectra can be simultaneously fitted by a model with $S^A_{vib}(Q_x)$ = 0.76 (λ^A = 643 cm^{-1}), with an effective Herzberg-Teller reorganization energy [Eq. (8)] of λ^{HT} = 450 cm^{-1} at 4.5 K and 947 cm^{-1} at 290 K [Fig. 4(c), Table II, supplementary material Table S1].

Table II explores whether the Herzberg-Teller Q_x intensity is *x*-polarized and/or *y*-polarized. If *y*-polarized, then the spectral fits indicate that 45% of the Q_x intensity is *y*-polarized at 4.5 K, increasing to 59% at 290 K.

The polarization of the Q_x band could, in principle, be measured using linear dichroism techniques, but to date this difficult technique has not been applied to Pheo-a. Polarization information can also be extracted from commonly applied MCD techniques. Currently feasible analyses rely on the assumption that the Q bands only interact within themselves and not the Soret band. Ignoring the possibility of Q_x vibronically coupling with B_x or B_y, it is possible[32] to analytically invert MCD and absorption data to obtain polarization information. Such an analysis therefore assumes that all of the Herzberg-Teller intensity in Q_x is *y*-polarized. A previous analysis[32] of Pheo-a in MeOH/EtOH at 1.5 K (see supplementary material Sec. S2) using this approach indicated that $S^A_{vib}(Q_x)$ = 0.2 and the fraction of *y*-polarized intensity is 53%. Unfortunately, this estimate of the Huang-Rhys factor is much less than the value of 0.76 coming from the model fits, indicating that it is not valid to assume that all of the Herzberg-Teller intensity is *y*-polarized. Hence, based on all currently available experimental information, it appears that $S^A_{vib}(Q_x)$ is in the range 0.2–0.8 while the band is at most 50% polarized in the *y*-direction. We will subsequently consider CAM-B3LYP predictions for this quantity.

The presence of the Herzberg-Teller intensity amongst the Q_y(1–0) band is also anticipated.[2] Based on analytical inversion of MCD and absorption data[32] (see supplementary material Sec. S1), its contribution to the intensity is determined to mimic an effective Huang-Rhys factor of 0.03. Using this correction, the best-estimate for $S^A_{vib}(Q_y)$ is therefore 0.40.

B. High resolution fluorescence and fluorescence excitation spectra of Pheo-a

The high-resolution vibrational structure of Q_y was revealed by spectral hole burning (HB) and ΔFLN, as reviewed in Ref. 58. The intramolecular vibrational modes belonging to the ground electronic state were found by the ΔFLN method[28] applied at 4.5 K. The IDF of the transition energies was determined by spectral HB action spectroscopy at unchanged laser intensity. The IDF peaked at 669.5 ± 0.3 nm and showed a width of 220 ± 30 cm^{-1}.

Figure 6 shows the ΔFLN spectrum of Pheo-a recorded with 6 cm^{-1} spectral resolution. It reveals a distinct ZPL at the origin accompanied by a wide PSB and a multitude of sharp vibrational sidelines shifted away from it toward lower energies. More than 47 ground-state intramolecular vibrational modes between 125 and 1700 cm^{-1} were detected. From the ratio of the ZPL intensity to the PSB intensity [see Eq. (1)], a strength of electron-phonon coupling equal to S_{ph} = 0.64 ± 0.08 was estimated.

In addition, the Q_y excited state vibrational modes are revealed in Fig. 5(a) from fluorescence spectra obtained following selective excitation into the 565–650 nm vibrational sideband (the excitation range highlighted in Fig. 3). Precise energetic resonance between

TABLE II. Various interpretations of the Q_x absorption of Pheo-a based on Franck-Condon (FC) 6-mode fits spectra, possibly with 3 additional Herzberg-Teller (HT) allowed modes, CAM-B3LYP calculations, and MCD analytical data inversion;[32] see Figs. 4 and 9, and Table S1.

	4.5 K					290 K				
	FC		HT			FC		HT		
Method	$S^A{}_{vib}$	λ^A (cm^{-1})	λ^{HT}_x (cm^{-1})	λ^{HT}_y (cm^{-1})	%*y*	$S^A{}_{vib}$	λ^A (cm^{-1})	λ^{HT}_x (cm^{-1})	λ^{HT}_y (cm^{-1})	%*y*
MCD data inversion[a]	0.2		[0]		53					
6 FC mode fit	1.57	1540	[0]	[0]	[0]	2.06	1960	[0]	[0]	[0]
6 FC + 3 HT mode fit	0.76	640	0	450	45	0.76	640	0	95	59
6 FC + 3 HT mode fit	0.76	640	450	0	0	0.76	640	950	0	0
CAM-B3LYP unscaled	0.87	780	460	210	13					
CAM-B3LYP scaled[b] × 1.2, 1.2, 1.2	2.40[c]	1120	660	300	15					
CAM-B3LYP scaled[b] × 1, 0, 2.5	1.67[c]	780	0	1300	48					
CAM-B3LYP scaled[b] × 1, 1.7, 0	1.67[c]	780	1320	0	0					

[a]At 1.5 K in MeOH/EtOH,[32] obtained assuming that the Soret bands do not couple with Q_x.
[b]Three scaling actors are listed, for in order: the Franck-Condon displacements δ, the *x*-polarized transition-moment derivatives, and the *y*-polarized transition-moment derivatives.
[c]Neglecting modes <100 cm^{-1} that have no effect of the spectrum at this resolution, S^A becomes 1.28 when scaled uniformly by ×1.2 and 0.87 when unscaled.

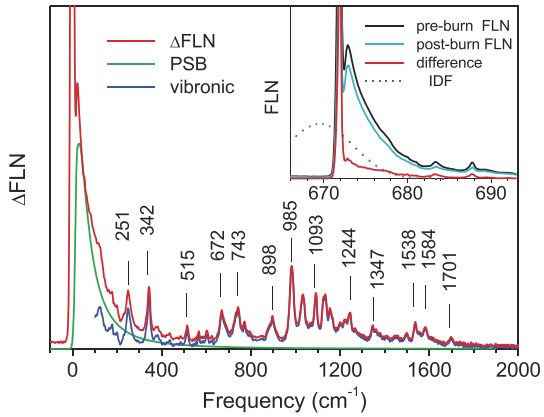

FIG. 6. ΔFLN spectrum (red) of Pheo-a in TEA glass at 4.5 K shown relative to the ZPL origin. The purely vibrational component (blue) is revealed by subtracting the model phonon contribution (PSB, green) from the ΔFLN spectrum. Fluorescence excitation and hole-burning were performed at 671.9 nm, at the red side of the Q_y absorption spectrum; see Fig. 3. The inset explains the ΔFLN measurement: black and blue curves denote the preburn and postburn FLN spectra recorded with low fluencies of 3.3 mJ/cm^2, while the postburn spectrum was measured after the intermediate hole-burning stage with a fluence of 121 mJ/cm^2.

the excitation laser and the sideband transitions boosts fluorescence in the 0–0 transition region only from a small subensemble of molecules in the total inhomogeneously broadened ensemble. More than 38 modes between 125 and 1600 cm^{-1} were detected by this method.

The vibrational mode frequencies, Huang-Rhys factors, and related reorganization energies in the ground and excited electronic states are collected in Table III. One can see that the nature of the strongly displaced vibrational modes in the excited and ground electronic states is quite different, underscoring the breakage of the mirror symmetry rule.

The data in Table III look similar to that for Chl-a,[2–4] except the distribution of frequencies of the more intense modes, which in Pheo-a is shifted toward smaller frequencies by about 200 cm^{-1}.

TABLE III. Vibrational frequencies ν_j (±3 cm^{-1}), Huang-Rhys factors[a] S_j (±0.0008), and reorganization energies λ_j of Pheo-a in TEA determined from ΔFLN measurements (ground state) and selective-excitation fluorescence measurements (excited Q_y state) at 4.5 K.

Ground state vibrations			Excited state vibrations[b]		
ν_j (cm^{-1})	S_j	λ_j (cm^{-1})	ν_j (cm^{-1})	S_j	λ_j (cm^{-1})
123	0.0181	2.2	127	0.0154	2.0
176	0.0088	1.6	181	0.0051	0.9
201	0.0019	0.4	198	0.0045	0.9
251	0.0161	4.1	250	0.0270	6.8
342	0.0149	5.1	341	0.0327	11.2
378	0.0058	2.2	375	0.0071	2.7
431	0.0030	1.3	426	0.0010	0.4
485	0.0019	0.9	459	0.0023	1.1
515	0.0050	2.6	514	0.0083	4.3

TABLE III. (*Continued.*)

Ground state vibrations			Excited state vibrations[b]		
ν_j (cm^{-1})	S_j	λ_j (cm^{-1})	ν_j (cm^{-1})	S_j	λ_j (cm^{-1})
544	0.0015	0.8			
566	0.0029	1.6	565	0.0039	2.2
580	0.0019	1.1			
603	0.0044	2.6	601	0.0045	2.7
624	0.0025	1.5	626	0.0027	1.7
654	0.0021	1.4			
672	0.0150	10.1	673	0.0148	10.0
690	0.0042	2.9			
732	0.0093	6.8	737	0.0161	11.9
743	0.0117	8.7			
772	0.0082	6.3	770	0.0180	13.9
796	0.0028	2.2	797	0.0006	0.5
846	0.0048	4.1	844	0.0026	2.2
884	0.0044	3.9	879	0.0013	1.1
898	0.0163	12.0			
913	0.0044	4.0	908	0.0032	2.9
985	0.0403	39.7	984	0.0071	7.0
1034	0.0344	35.6	1024	0.0011	1.1
1093	0.0284	31.1	1059	0.0045	4.8
1126	0.0115	13.0	1073	0.0071	7.6
1135	0.0144	16.4	1098	0.0039	4.3
1157	0.0146	16.9	1117	0.0077	8.6
1168	0.0076	8.9	1152	0.0031	3.6
1202	0.0072	8.6	1198	0.0045	5.4
1224	0.0095	11.6	1240	0.0013	1.6
1244	0.0126	15.7	1265	0.0045	5.7
1267	0.0067	8.5	1294	0.0302	39.1
1347	0.0079	10.7	1362	0.0128	17.4
1363	0.0074	10.1	1380	0.0154	21.3
1379	0.0051	7.0	1407	0.0006	0.8
1412	0.0038	5.3	1427	0.0026	3.7
1451	0.0066	9.6	1471	0.0006	0.9
1501	0.0055	8.3	1512	0.0071	10.7
1538	0.0114	17.5	1540	0.0276	42.5
1557	0.0011	1.7			
1584	0.0094	14.8	1575	0.0327	51.5
1612	0.0037	6.0			
1701	0.0041	6.9			
Sum	0.425	395		0.346	317

[a]Derived ignoring possible effects of Duschinsky rotation on line intensities other than those that differentiate the absorption and emission Huang-Rhys factors.
[b]Strong similarity to previous more qualitative fluorescence-excitation measurements.[7]

The total Huang-Rhys factors determined from the high-resolution data of $S^A_{vib} = 0.43$ and $S^E_{vib} = 0.35$ are in excellent agreement with previous determinations based on the analysis of the low-resolution fluorescence spectrum, indicating self-consistency of the quite different data analysis techniques applied. The corresponding reorganization energies $\lambda^A_{vib} = 395$ cm^{-1} and $\lambda^E_{vib} = 317$ cm^{-1} are similarly analogous. In greater detail, the obtained distributions of the Huang-Rhys factors from the high-resolution and low-resolution spectra

are compared in supplementary material, Sec. S5. The electron-vibration coupling in Pheo-a can be considered weak, as in Chl-a and bacteriochlorophyll-a, because both S^A_{vib} and S^E_{vib} are significantly less than 1.

IV. COMPUTATIONAL RESULTS AND DISCUSSION

A. Computational prediction of Q_y absorption and emission spectra

The reorganization energies associated with chlorophyll spectroscopy are relatively very low (as they need to be in order to avoid large energy loss during photosynthesis), making their accurate calculation difficult. As a result, computational methods can give order-of-magnitude errors,[43] something not commonly seen given the sophistication level of modern approaches. From amongst density-functional approaches, only methods including long-range correction are naively considered appropriate[59] since other methods typically erroneously predict non-Gouterman states in the critical spectral region between the Q and Soret bands.[60] These states interfere with the states of interest, distorting equilibrium geometries and hence spectral lineshapes. Because Q_x is much higher in energy than Q_y for Pheo-a, such effects are expected to be more serious than for other small-gap molecules such as Chl-a. For the analogous large-gap situation in bacteriochlorophyll-a, for the Q_y band, we found[43] that CAM-B3LYP[44,45] predicted results very close to those observed, B3LYP[48] gave useful results, but all other methods used therein failed to even qualitatively depict the spectra. B3LYP has been found to be useful for other chlorophylls also.[61] Nevertheless, CAM-B3LYP is expected to be more reliable as it is designed to handle charge-transfer states. Surveying the energies of many states with and without charge transfer, the predictions of CAM-B3LYP concerning (absolute) origin energies have recently been noted as performing amongst the best of the non-double-hybrid approaches.[62]

In Fig. 7, the observed low-resolution Q_y absorption and emission spectra at 4.5 K in TEA (with the absorption reflected about the origin) are compared to computational predictions of Franck-Condon-allowed spectra obtained using 10 different methods as follows: *ab initio* Hartree-Fock[54] (HF) and configuration-interaction singles[55,63] (CIS) as well as their semiempirical PM6 equivalents;[53] the generalized-gradient approximation density-functional PBE;[52] the hybrid density functionals PBE0,[49] HSE06,[50,64] and B3LYP;[48] the meta generalized-gradient method MN15;[51] and the long-range corrected hybrid functionals LC-ωhPBE,[47] ωB97XD,[46] and CAM-B3LYP.[44,45]

Table IV summarizes the results, listing the reorganization energies calculated by the computational structure methods directly as the difference in the vertical and adiabatic excitation energies [Eq. (6)] and those as modeled using curvilinear and rectilinear harmonic descriptions of the potential-energy surfaces. The curvilinear approach includes many terms, often critical in nature, that appear as anharmonic contributions to the potential energy in traditional rectilinear expansions, at the expense of introducing, usually small and ignorable, anharmonic contributions to the kinetic energy.[65,66] It does not include all anharmonic terms, however, and so will not be guaranteed to provide a useful description of the potential-energy surfaces over all regions of interest. As discussed later, some computational methods depict unexpected chemical features, and in these cases, the curvilinear approach can severely misrepresent the potential-energy surface, manifesting 4-fold errors in its perceived reorganization energy compared to the value from direct evaluation, but otherwise errors are below 4%. However, when rectilinear coordinates are used, the errors range from 8% to 261% in the well-behaved cases and up to a factor of 24 when the chemistry is poorly described. Nevertheless, rectilinear approaches remain in common use, e.g., in the current version of Gaussian-16.[38,62,67] Rectilinear approaches work well if the molecule of interest does not undergo any large-scale bending or torsional motions as a result of the electronic transition, peripheral methyl rotation, etc.[40]

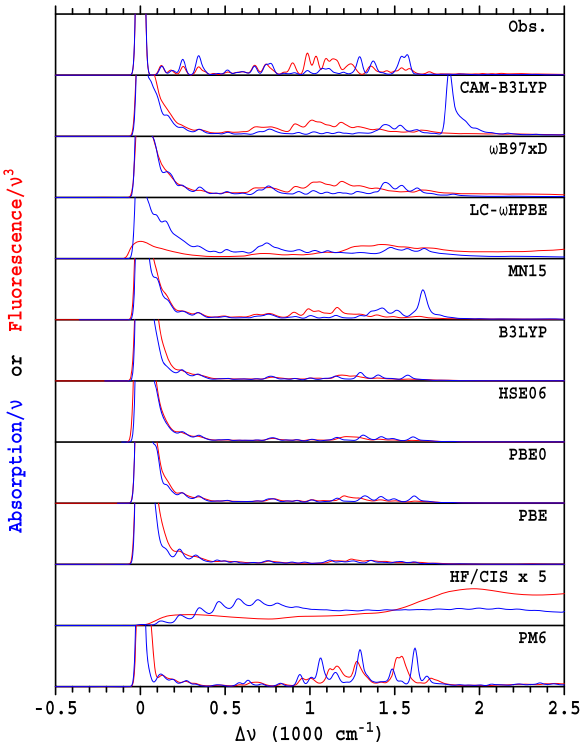

FIG. 7. Comparison of Franck-Condon calculated reflected emission (red) and absorption (blue) spectra of Me-Pheo-a with simulated spectra based on the observed data in Table III for Pheo-a in TEA at 4.5 K. The spectra all embody inhomogeneous broadening of σ = 15 cm^{-1} are normalized with respect to area and focus only on the vibrational sideband part.

Before proceeding, we consider another approximation used in the calculations: the substitution of methyl for phytyl. Indeed, small effects have been measured when phytyl is replaced with H,[68–70] a substitution that introduces carboxylic-acid functionality. Herein, we replace phytyl with methyl. This approximation was tested using CAM-B3LYP and found to have no significant influence on reorganization energies, data analysis, or calculated spectra (Table IV).

From Table IV, it is clear that none of the methods used provided a qualitatively correct description of the experimental

TABLE IV. Calculated Me-Pheo-a Q_y reorganization energies, in cm^{-1}, unscaled, for absorption and emission.

	Emission[a] λ^E			Absorption[b] λ^A					
	Total			Total			$6b_{3u}$–like mode		
Method	Direct[c]	Curvi.[d]	Recti.[e]	Direct[c]	Curvi.[d]	Recti.[e]	ν	λ	Total corrected
CAM-B3LYP[f]	481	598	658	1214	1 360	1 444	1818–1854[g]	895	465
ωB97XD	594	780	830	1609	2 012	2 088	1960	1 537	475
LC-ωHPBE	1817	3094	3 200	4768	17 100	17 200			
MN15	282	302	317	493	492	534			
B3LYP	165	170	290	184	183	317			
HSE06	164	170	210	183	183	238			
PBE0	178	182	210	207	203	247			
PBE	159	162	359	207	139	354			
HF/CIS	3656	6279	93 300	4130	17 000	104 300	2522	14 830	2141
PM6	741		442	878		707			

[a]Observed Pheo-a λ^E = 395 cm^{-1} and 401 cm^{-1} from high-resolution and low resolution data, respectively.
[b]Observed Pheo-a λ^A = 317 cm^{-1} and 344 cm^{-1} from high-resolution and low resolution data, respectively.
[c]Vertical to adiabatic energy difference from direct calculation, Eq. (6).
[d]From curvilinear harmonic approximation to the potential-energy surfaces, used to simulate the spectra in Fig. 7.
[e]From rectilinear harmonic approximation to the potential-energy surfaces, not used in any analysis.
[f]CAM-B3LYP calculations for Pheo-a instead of MePheo-a: λ^E = 480 cm^{-1} (raw), 595 cm^{-1} (curvi.), 658 cm^{-1} (recti.), λ^E = 1212 cm^{-1} (raw), 1356 cm^{-1} (curvi.), 1444 cm^{-1} (recti.).
[g]Primary mode at 1818 cm^{-1}, split slightly by Fermi resonance.

spectra, with some errors in the reorganization energies found to exceed two orders of magnitude, but simple modifications of the CAM-B3LYP and ωB97XD approaches (and possibly also MN15) do lead to useful results that we apply to interpret the observed data.

The B3LYP, HSE06, PBE, and PBE0 methods all underestimate the reorganization energies by of order a factor of two, and similarly, all predict that the reorganization energy in emission λ^E exceeds that in absorption λ^A, contrary to observation (Table IV). PM6 overestimates the reorganization energies and fails to predict the observed absorption-emission asymmetry. MN15 slightly underestimates λ^E while overestimating λ^A. Of all the methods considered, its predicted spectra in Fig. 7 appear closest to the observed spectra, but there is too much displacement in some high-frequency modes in absorption. It is conceivable that this method could be used to provide a basic interpretation of the observed spectra, but we do not take this route, focusing instead on the CAM-B3LYP and ωB97XD alternatives. These methods also predict spectra resembling those observed, except for too much displacement in absorption in one high-frequency mode. The same mode has a catastrophic effect upon the HF/CIS predictions. For CAM-B3LYP, ωB97XD, HF/CIS, and MN15, the poorly represented modes are described and discussed in detail in supplementary material, Sec. S6. Except for MN15, this mode is analogous to the $6b_{3u}$ mode of porphyrin[71] and is related to the Kekulé mode of benzene, ν_{14}.[72] It controls aromaticity in these compounds,[73] with CAM-B3LYP, ωB97XD, and CIS predicting an excessive frequency increase (see supplementary material, Sec. S6),[73] owing to excessive bond localization in the Q_y state. This effect does not occur in analogous calculations of the ground state or the Q_x state. In the supplementary material, this is explained as arising from vibronic coupling between Q_y and two charge-localized (n, π^*) states involving the nitrogen lone-pair state (absent in chlorophylls), couplings that in porphyrin are symmetry-forbidden for Q_x. For MN15, the erroneous displacement is in a mode involving the same type of *meso*-carbon CC stretches but has a different pseudosymmetry.

As CAM-B3LYP was able to describe absorption-emission asymmetry in the Q_y spectra of bacteriochlorophyll-a in considerable detail, we continue using this computational method only. However, results for the $6b_{3u}$-like mode were omitted from subsequent analyses. The effect of this is highlighted in Table IV, giving reorganization energies reminiscent of those observed, including the important prediction that the reorganization energy in emission exceeds that in absorption. Also, the CAM-B3LYP force constants in internal coordinates are scaled by factors of 0.95 for stretch and band motions and 0.99 for torsional motions, values fitted to reproduce high-resolution data for porphyrin.[43] A detailed comparison on the absorption and emission lines observed and calculated using CAM-B3LYP is presented in Table V. While the comparison is not quantitative, most of the observed lines appear to have their counterparts from the calculated results. It therefore seems reasonable to suggest that the cause of the calculated absorption/emission asymmetry reflects reality.

In the supplementary material, a full listing is provided of the CAM-B3LYP calculated normal modes for the ground, Q_y, and Q_x states of MePheo-a, analyzed each in terms of the fraction of in-plane, out-of-plane, stretch, bend, and torsional contributions. The associated vibrational displacements, reorganization energies, and Duschinsky matrices for the Q_x and Q_y transitions are also listed.

TABLE V. Comparison of all observed Pheo-a and scaled[a] CAM-B3LYP-calculated Me-Pheo-a Q_y absorption and emission lines with $\lambda > 9$ cm^{-1} in either the observed or calculated data, seeking connections of the form: observed emission line → calculated emission line → mapped onto calculated absorption line → observed absorption line.

Emission (S_0)				Q_y assignment in terms of S_0 modes[b]		Absorption (Q_y)			
Observed		CAM-B3LYP				CAM-B3LYP		Observed	
ν (cm^{-1})	λ (cm^{-1})	ν (cm^{-1})	λ (cm^{-1})	% wt.	% δ	ν (cm^{-1})	λ (cm^{-1})	ν (cm^{-1})	λ (cm^{-1})
		337	6	97	97	334	7	341	11
672	10	655	19	44	310	659	2		
743	9	728	11	65	96	725	11	673	10
		755	8	76	130	753	5	737	12
								770	14
898	12	869	23	53	330	873	3		
985	40	948, 952	25, 14	21,76	−170, 240	949	1		
1034	36	974	34	80	147	972	11		
1093	31	1010+	14	45	−280	992	4		
		1079	14						
1126	13	1122	11	66	250	1120	2		
1135	16	1132	38	58	160	1114	4	1117	9
1157	17								
1168	9								
1202	9	1222	18						
1224	12	1231	11	87	110	1230	6		
1244	16	1262	6	71	100	1260	5		
		1320	6	41	−107	1298	9	1294	39
1348	11	1341	8	37	−106	1338	12		
1363	10	1345	8	27	−510	1340	1		
		1365	1.4	24	−22	1361	19	1362	17
		1465	1.4	45	19	1364	26	1380	21
1451	10	1433	6	34	101	1409	3		
1538	18	1508	11						
		1388	0.0	27	1	1393[c]	21	1509	11
		1458	1.8	40	22	1455[c]	31	1538	42
1584	15	1573	23	45	69	1554[c]	17	1573	51

[a]Force constant matrix scaled in internal coordinates by factors of 0.95 for stretch motions, 0.95 for bend motions, and 0.99 for torsional motions. After scaling, the total reorganization energies become $\lambda^E = 542$ cm^{-1} and $\lambda^A = 1231$ cm^{-1} (423 cm^{-1} after removal of $6b_{3u}$-like mode[b]); see Table IV.

[b]Assignment is taken to be the S_0 mode that makes the greatest percentage contribution D_{kj}^2 to the Q_y mode (wt.) and the contribution from Eq. (12) that the modes make to the Q_y displacement (δ).

[c]Excluding the $6b_{3u}$-like mode at 1727 cm^{-1} ($\lambda = 764$ cm^{-1} and its two satellites at 1754 cm^{-1} and 1763 cm^{-1} with $\lambda = 30$ cm^{-1} and 13 cm^{-1}, respectively). These poorly represented modes could distort the calculated absorption of nearby modes.

B. Understanding the Q_y absorption and emission asymmetry

Typical of molecular spectroscopy is the observation that absorption and emission spectra take on mirror symmetry. This expectation is based on the assumption that shapes of the two potential-energy surfaces are identical harmonic functions, the surfaces varying only by displacements in energy and in equilibrium position. Mirror symmetry is lost whenever significant changes in vibration frequency, in the form of the normal modes of vibration, or substantial anharmonicity are involved. For bacteriochlorophyll-a, we found that its large absorption-emission asymmetry could be accounted for by changes to the form of the normal modes between the ground state S_0 and the Q_y excited state.[43] From the DFT calculations, the displacements in each normal mode j of the final electronic state (S_0 for emission and Q_y for absorption) are evaluated as

$$\delta_j^E = \left(\frac{h}{\nu_j^E}\right) \sum_i C_{ij}^E m_i^{1/2} \Delta x_i$$

and

$$\delta_j^A = \left(\frac{h}{\nu_j^A}\right) \sum_i C_{ij}^A m_i^{1/2} \Delta x_i, \tag{10}$$

where Δx_i is the change in equilibrium value of a Cartesian coordinate associated with an atom of mass m_i, while **C** are the unitary

matrices specifying the final-state normal coordinates and vibration frequencies ν_j, evaluated by diagonalizing the mass-weighted Hessian matrix of the final state.

The Duschinsky rotation matrix

$$\mathbf{D} = \left(\mathbf{C}^E\right)^T \mathbf{C}^A \tag{11}$$

can be used to express the displacements on one state in terms of those on the other, within the harmonic approximation. This leads to, for example,

$$\delta_j^A = \left(\frac{h}{\nu_j^A}\right) \sum_k D_{kj} \left(\frac{\nu_k^E}{h}\right) \delta_k^E, \tag{12}$$

which allows the displacement of mode j in absorption to be expressed in relation to displacement of the modes k in emission, noting that the Huang-Rhys factors depicting intensities are the square of these displacements [Eq. (9)] and hence this sum explicitly embodies interference effects. The Duschinsky matrix is orthogonal when expressed in terms of rectilinear coordinates only. For the curvilinear coordinates used herein, orthogonalization of the matrix is performed prior to use.[41] This is an approximate procedure needed when molecules can undertake large-amplitude motions; the results are qualitatively similar to those obtained using traditional rectilinear analyses, but the details often differ.

The purpose of Table V is to seek connections from observed lines in emission to calculated lines in emission, then through Eq. (12) to calculated lines in absorption, and finally to observed lines in absorption. Such connections provide a detailed quantitative model interpreting the observed absorption-emission asymmetry. In only 3 cases are such complete connections established, connecting the observed emission lines at 743, 1135, and 1584 cm^{-1} to observed absorption lines at 673, 1117, and 1573 cm^{-1}, respectively. The connection is most clearly seen for the lowest-frequency mode mentioned. It is observed in emission at 743 cm^{-1}, with $\lambda = 9$ cm^{-1}, and appears to correlate with a calculated mode at 728 cm^{-1}, with $\lambda = 11$ cm^{-1}. According to the Duschinsky matrix, this mode contributes 65% by weight to a calculated absorption line at 725 cm^{-1}, with $\lambda = 11$ cm^{-1}, and appears to correlate with an observed mode at 673 cm^{-1}, with $\lambda = 10$ cm^{-1}. From Eq. (12), 96% of its displacement δ_j^A arises from just this one contribution, δ_k^E. The connection between the highest-frequency pair (1584 cm^{-1} in emission, 1573 cm^{-1} in absorption) also appears sound, but now one S_0 mode contributes 45% to the weight and 69% to the displacement of the Q_y mode. For the third pair (1135 cm^{-1} in emission, 1117 cm^{-1} in absorption), one mode contributes 58% to the weight but 160% to the shift, indicating that quantum mechanical interference between different contributions is also important.

To understand interference effects, Fig. 8 shows the calmative weight and calmative relative contribution of δ_k^E contributions to δ_j^A for 6 Q_y modes. The expectation of mirror symmetry comes from approximating the Duschinsky matrix with the unit matrix, making all curves in Fig. 8 take on the form of Heaviside-step functions. For the calculated absorption line at 1554 cm^{-1}, mirror symmetry with the emission line at 1573 cm^{-1} is apparent, connecting the aforementioned observed lines at 1584 cm^{-1} in emission and 1573 cm^{-1} in absorption. In contrast, for the observed pair at 1135 cm^{-1} in emission (strong) and 1117 cm^{-1} in absorption (weak), the intensity from the corresponding calculated Q_y line at 1114 cm^{-1} has its 160% contribution from the dominate S_0 mode canceled by destructive interference coming from very many other modes.

Indeed, the top row of images in Fig. 8 is an example of how destructive interference between intense emission processes results in the corresponding absorption lines being weak, mostly too weak to observe. Most intense lines in absorption do not

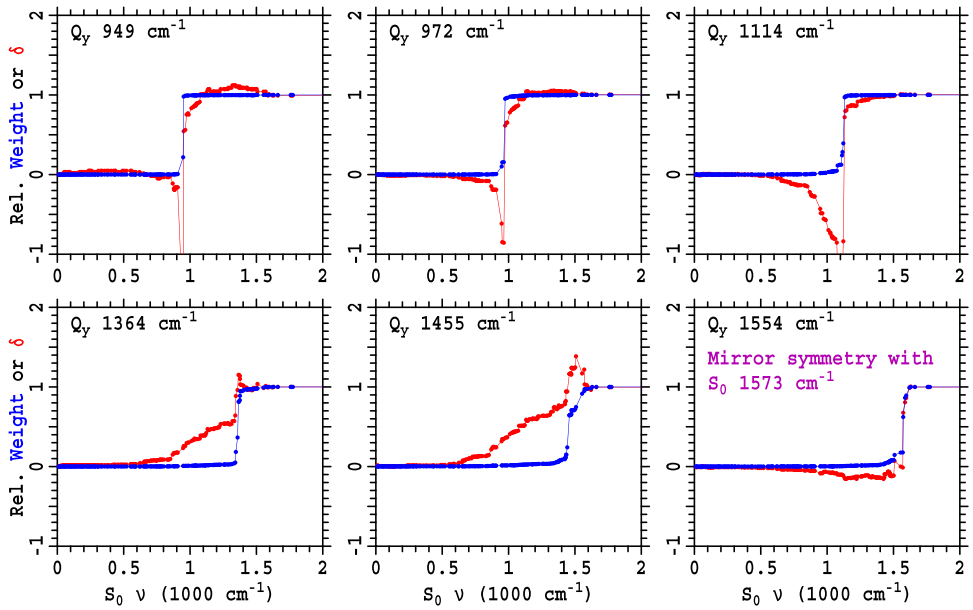

FIG. 8. Origin of absorption-emission asymmetry in Q_y of MePheo-a according to CAM-B3LYP calculations (with scaled force constants, see Table V), showing calmative contributions of each S_0 mode to various Q_y mode and its displacement. Weak absorption of Q_y at 949, 972, and 1114 cm^{-1} (top row) arises through cancellation of contributions associated with intense emission lines, while strong absorption of Q_y at 1364, 1455, and 1554 cm^{-1} (bottom row) arises in the first two cases from manifold contributions from modes that are each weak in emission; only for the 1554 cm^{-1} mode is there a close correspondence between modes strong in both absorption and emission, as anticipated by mirror symmetry.

correspond to intense lines in emission. The bottom row of images in the figure is an example of how intensity arises for some of the strong absorption lines. In two cases (calculated absorption lines at 1364 cm^{-1} and 1455 cm^{-1}, assigned to observed lines at 1380 cm^{-1} and 1538 cm^{-1}), no corresponding strong lines in emission are identified, with the absorption intensity arising from constructive interference involving many modes, each themselves with only weak emission intensity. Hence, no symmetry between absorption and emission spectra is predicted, consistent with the experimental observations. These results closely parallel those found previously for bacteriochlorophyll-a.[43]

C. Predicting the relative *x*- and *y*-polarized contributions to the Q_x and Q_y absorptions

CAM-B3LYP was used to predict the Herzberg-Teller contributions to the Q_y and Q_x transitions by numerical evaluation of the dipole derivatives in Eq. (7), with the derivatives listed in supplementary material, Table S2. Calculated spectra, including the Franck-Condon contributions, are then compared to the observed ones in Fig. 9.

For Q_y, the observed data presented are the *x* and *y* components at 1.5 K in MeOH/EtOH obtained by analytical MCD data

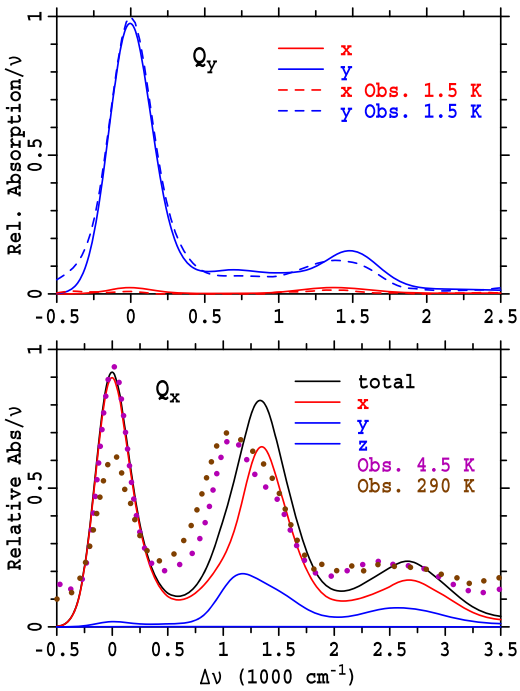

FIG. 9. Comparison of (unscaled) CAM-B3LYP calculated *x*-polarized and *y*-polarized intensity for MePheo-a involving both the Franck-Condon and Herzberg-Teller mechanisms (solid lines) with experimental spectra of Pheo-a (dashed lines or points). For Q_y, the observed data are the component-resolved results obtained at 1.5 K in MeOH/EtOH through analytical MCD data inversion,[32] whereas for Q_x the spectra from Fig. 4 observed in TEA at 4.5 K and at 290 K are used from Figs. 2 and 3, respectively. The calculated spectra include an inhomogeneous broadening of 103 cm^{-1} for Q_y and 133 cm^{-1} for Q_x.

inversion,[32] with the anomalous mode described in supplementary material, Sec. S6, not included in the calculated spectrum. Such calculations qualitatively describe the observed spectra and have λ^A = 465 cm^{-1} (Table IV), λ_x^{HT} = 42 cm^{-1}, and λ_y^{HT} = 20 cm^{-1}. The Herzberg-Teller coupling is too weak to perturb the Franck-Condon-only spectrum calculated for the primary *y* polarization and can be neglected, as is usually assumed. However, the *x* intensity in the Q_y transition appears to be too great, with the calculated dipole derivatives needing to be scaled by a factor of 0.75 in order to predict the same degree of *x*-polarization as deduced from the analytical MCD analysis.[32]

As shown in Fig. 9, for Q_x, the observed data at 4.5 K and at 290 K (Fig. 4) are very different from that observed for Q_y, and the calculated spectra reflect these changes. The differences arise owing to the calculated large increases in the Franck-Condon displacements (λ^A increases from 465 cm^{-1} to 776 cm^{-1}) and the Herzberg-Teller intensity (λ_x^{HT} increases from 42 cm^{-1} to 460 cm^{-1} and λ_y^{HT} increases from 20 cm^{-1} to 210 cm^{-1}), as listed in Table II. However, the close similarity found between the calculated and the observed spectra for Q_y is not reproduced for Q_x. The most significant issue for Q_x concerns the fraction of the intensity that is *y*-polarized, with CAM-B3LYP predicting this to be 13%. As discussed before, from the analytical MCD data inversion of the Q_x spectra,[32] the expected fraction is 53% (Table II). However, the MCD data analysis is based on the assumption that only the Q_x and Q_y states are strongly vibronically coupled together, whereas the CAM-B3LYP prediction of λ_x^{HT} = 460 cm^{-1} is indicative of very strong coupling between Q_x and B_x. Hence, the analytical MCD data inversion method used is not expected to be reliable for Q_x. In supplementary material, Sec. S8, three simple rescaling schemes for the CAM-B3LYP data are described that produce enhanced agreement with the observed data, with the resulting properties listed in Table II. In these modifications, the proportion of *y* polarization in Q_x ranges from 0% to 48%. It is therefore difficult to make a robust interpretation of the experimental data based on the calculated properties.

V. CONCLUSIONS

In this work, the vibrational structure of the optical absorption and fluorescence spectra related to two lowest-energy singlet electronic states of Pheo-a, Q_y and Q_x, were studied by combined experimental and quantum chemical analyses, as well as spectral simulation methods. Both low-resolution and high-resolution experiment techniques were applied, delivering spectroscopic parameters in excellent accord. The Q_y absorption and emission bands are demonstrated to be very asymmetric, an effect attributed to subtle Duschinsky rotation effects that remove the expected correlation between the forms of the normal vibrational modes that dominate absorption and emission intensities. The Q_x band structure is shown to be environmentally sensitive, with an absorption profile that cannot be interpreted based on the Franck-Condon principle and its associated Huang-Rhys factors. Instead, the band profile is dominated by the Herzberg-Teller intensity. The polarization of this intensity was not accurately determined, with the viable range being anywhere between 0% and 53% *y* polarization. CAM-B3LYP calculations predict that Q_x is 13% *y*-polarized, but the method

only qualitatively depicts the observed bandshape, making this an unreliable estimate.

In regard to the computational methods applied, great variations in predicted spectral properties resulted, owing to the subtle nature of the chemical effects that control the spectra. While CAM-B3LYP was successfully applied to interpret key properties of both Q_x and Q_y, its application to Q_y required the empirical neglect of a significant displacement in the Q_y state involving a Kekulé-like[72] mode akin to the $6b_{3u}$ mode of porphyrin.[71] This mode is of anomalously high frequency,[73] controls aromaticity,[73] and is poorly represented by CAM-B3LYP, ωB97XD, and CIS in the Q_y state. Its properties appear to arise owing to vibronic coupling between Q_y and localized nitrogen lone-pair (n, π^*) excited states, states that do not exist for chlorophylls, with the wrong underlying symmetries to couple to Q_x for pheophytins. The MN15 method appears to give reasonable results for most modes and may prove to be a useful alternative to range-corrected hybrid functionals like CAM-B3LYP, but that needs to be confirmed by further studies as the traditional hybrid and generalized-gradient methods that were considered failed to qualitatively describe the spectra.

SUPPLEMENTARY MATERIAL

See supplementary material for (1) supplementary information text and figures, (2) full listing of the CAM-B3LYP/6-31G* normal modes for S_0, Q_y, and Q_x of MePheo-a, and (3) structure, normal-coordinate definitions, Duschinsky matrices, and displacement vectors determined in curvilinear coordinates from CAM-B3LYP/6-31G* calculations of absorption and emission of MePheo-a involving Q_x and Q_y.

ACKNOWLEDGMENTS

This work was supported by the Estonian Research Council (Grant Nos. PRG539 and PSG264). The contribution of Dr. Eero Talts (Estonian University of Life Sciences) to the sample preparation is highly appreciated. We thank also the Australian Research Council for funding through Grant No. DP150103137.

REFERENCES

[1] R. van Grondelle, J. P. Dekker, T. Gillbro, and V. Sundström, Biochim. Biophys. Acta **1187**, 1 (1994).
[2] J. R. Reimers, Z.-L. Cai, R. Kobayashi, M. Rätsep, A. Freiberg, and E. Krausz, Sci. Rep. **3**, 2761 (2013).
[3] J. R. Reimers, Z.-L. Cai, R. Kobayashi, M. Rätsep, A. Freiberg, and E. Krausz, Phys. Chem. Chem. Phys. **16**, 2323 (2014).
[4] M. Rätsep, J. Linnanto, and A. Freiberg, J. Chem. Phys. **130**, 194501 (2009).
[5] M. Gouterman, J. Mol. Spectrosc. **6**, 138 (1961).
[6] C. Houssier and K. Sauer, J. Am. Chem. Soc. **92**, 779 (1970).
[7] R. A. Avarmaa and K. K. Rebane, Spectrochim. Acta, Part A **41**, 1365 (1985).
[8] M. Fragata, B. Norden, and T. Kurucsev, Photochem. Photobiol. **47**, 133 (1988).
[9] D. Sundholm, Chem. Phys. Lett. **317**, 545 (2000).
[10] J. Hasegawa, Y. Ozeki, K. Ohkawa, M. Hada, and H. Nakatsuji, J. Phys. Chem. B **102**, 1320 (1998).
[11] A. B. J. Parusel and S. Grimme, J. Phys. Chem. B **104**, 5395 (2000).
[12] E. U. Condon, Phys. Rev. **32**, 858 (1928).
[13] K. Huang, A. Rhys, and N. F. Mott, Proc. R. Soc. London, Ser. A **204**, 406 (1950).
[14] G. Herzberg and E. Teller, Z. Phys. Chem. **21B**, 410 (1933).
[15] D. P. Craig, Nature **158**, 235 (1946).
[16] J. Jacobs, Proc. Phys. Soc., London, Sect. A **62**, 710 (1949).
[17] G. Orlandi and W. Siebrand, J. Chem. Phys. **58**, 4513 (1973).
[18] S. H. Lin and H. Eyring, Proc. Natl. Acad. Sci. U. S. A. **71**, 3802 (1974).
[19] S. B. Piepho, E. R. Krausz, and P. N. Schatz, J. Am. Chem. Soc. **100**, 2996 (1978).
[20] I. G. Ross, Isr. J. Chem. **14**, 118 (1975).
[21] P. J. Chappell, G. Fischer, J. R. Reimers, and I. G. Ross, J. Mol. Spectrosc. **87**, 316 (1981).
[22] G. Fischer, *Vibronic Coupling* (Academic Press, London, 1984).
[23] G. Fischer, J. R. Reimers, and I. G. Ross, Chem. Phys. **62**, 187 (1981).
[24] M. Born and R. Oppenheimer, Ann. Phys. **389**, 457 (1927).
[25] C. J. Ballhausen and A. E. Hansen, Annu. Rev. Phys. Chem. **23**, 15 (1972).
[26] T. Azumi and K. Matsuzaki, Photochem. Photobiol. **25**, 315 (1977).
[27] B. T. Sutcliffe and R. G. Woolley, J. Chem. Phys. **137**, 22A544 (2012).
[28] M. Rätsep and A. Freiberg, Chem. Phys. Lett. **377**, 371 (2003).
[29] M. Rätsep and A. Freiberg, J. Lumin. **127**, 251 (2007).
[30] M. Reppert, V. Naibo, and R. Jankowiak, J. Chem. Phys. **133**, 014506 (2010).
[31] J. Pieper, P. Artene, M. Rätsep, M. Pajusalu, and A. Freiberg, J. Phys. Chem. B **122**, 9289 (2018).
[32] J. R. Reimers and E. Krausz, Phys. Chem. Chem. Phys. **16**, 2315 (2014).
[33] F. Duschinsky, Acta Physiochim. U.R.S.S. **7**, 551 (1937).
[34] C. Eijckelhoff and J. P. Dekker, Photosynth. Res. **52**, 69 (1997).
[35] K. K. Rebane, *Impurity Spectra of Solids* (Plenum Press, New York, 1970).
[36] D. P. Craig and G. J. Small, J. Chem. Phys. **50**, 3827 (1969).
[37] G. J. Small, J. Chem. Phys. **54**, 3300 (1971).
[38] M. J. Frisch, G. W. Trucks, H. B. Schlegel, G. E. Scuseria, M. A. Robb, J. R. Cheeseman, G. Scalmani, V. Barone, G. A. Petersson, H. Nakatsuji, X. Li, M. Caricato, A. V. Marenich, J. Bloino, B. G. Janesko, R. Gomperts, B. Mennucci, H. P. Hratchian, J. V. Ortiz, A. F. Izmaylov, J. L. Sonnenberg, D. Williams, F. Ding, F. Lipparini, F. Egidi, J. Goings, B. Peng, A. Petrone, T. Henderson, D. Ranasinghe, V. G. Zakrzewski, J. Gao, N. Rega, G. Zheng, W. Liang, M. Hada, M. Ehara, K. Toyota, R. Fukuda, J. Hasegawa, M. Ishida, T. Nakajima, Y. Honda, O. Kitao, H. Nakai, T. Vreven, K. Throssell, J. A. Montgomery, Jr., J. E. Peralta, F. Ogliaro, M. J. Bearpark, J. J. Heyd, E. N. Brothers, K. N. Kudin, V. N. Staroverov, T. A. Keith, R. Kobayashi, J. Normand, K. Raghavachari, A. P. Rendell, J. C. Burant, S. S. Iyengar, J. Tomasi, M. Cossi, J. M. Millam, M. Klene, C. Adamo, R. Cammi, J. W. Ochterski, R. L. Martin, K. Morokuma, O. Farkas, J. B. Foresman, and D. J. Fox, GAUSSIAN 16, Revision A.03, Gaussian Inc., Wallingford, CT, 2016.
[39] J. J. P. Stewart, MOPAC2012, Stewart Computational Chemistry, Colorado Springs, CO, 2012.
[40] E. B. Wilson, J. C. Decius, and P. C. Cross, *Molecular Vibrations: The Theory of Infrared and Raman Vibrational Spectra* (McGraw-Hill Book Company, New York, 1955).
[41] J. R. Reimers, J. Chem. Phys. **115**, 9103 (2001).
[42] J. Bloino, A. Baiardi, and M. Biczysko, Int. J. Quantum Chem. **116**, 1543 (2016).
[43] M. Rätsep, Z.-L. Cai, J. R. Reimers, and A. Freiberg, J. Chem. Phys. **134**, 024506-1 (2011).
[44] T. Yanai, D. P. Tew, and N. C. Handy, Chem. Phys. Lett. **393**, 51 (2004).
[45] R. Kobayashi and R. D. Amos, Chem. Phys. Lett. **420**, 106 (2006).
[46] J.-D. Chai and M. Head-Gordon, Phys. Chem. Chem. Phys. **10**, 6615 (2008).
[47] T. M. Henderson, A. F. Izmaylov, G. Scalmani, and G. E. Scuseria, J. Chem. Phys. **131**, 044108 (2009).
[48] A. D. Becke, J. Chem. Phys. **98**, 5648 (1993).
[49] C. Adamo and V. Barone, J. Chem. Phys. **110**, 6158 (1999).
[50] A. V. Krukau, O. A. Vydrov, A. F. Izmaylov, and G. E. Scuseria, J. Chem. Phys. **125**, 224106 (2006).
[51] H. S. Yu, X. He, S. L. Li, and D. G. Truhlar, Chem. Sci. **7**, 5032 (2016).
[52] J. P. Perdew, K. Burke, and M. Ernzerhof, Phys. Rev. Lett. **77**, 3865 (1996).
[53] J. P. Stewart, J. Mol. Model. **13**, 1173 (2007).
[54] V. Fock, Z. Phys. **62**, 795 (1930).
[55] J. B. Foresman, M. Head-Gordon, J. A. Pople, and M. J. Frisch, J. Phys. Chem. **96**, 135 (1992).

[56]W. J. Hehre, R. Ditchfield, and J. A. Pople, J. Chem. Phys. **56**, 2257 (1972).
[57]F. Santoro, A. Lami, R. Improta, J. Bloino, and V. Barone, J. Chem. Phys. **128**, 224311 (2008).
[58]J. Pieper and A. Freiberg, in *The Biophysics of Photosynthesis*, edited by J. Golbeck and A. van der Est (Springer, 2014).
[59]Z.-L. Cai, M. J. Crossley, J. R. Reimers, R. Kobayashi, and R. D. Amos, J. Phys. Chem. B **110**, 15624 (2006).
[60]Z.-L. Cai, K. Sendt, and J. R. Reimers, J. Chem. Phys. **117**, 5543 (2002).
[61]M. Etinski, M. Petković, M. M. Ristić, and C. M. Marian, J. Phys. Chem. B **119**, 10156 (2015).
[62]F. Santoro and D. Jacquemin, Wiley Interdiscip. Rev.: Comput. Mol. Sci. **6**, 460 (2016).
[63]R. J. Buenker and J. L. Whitten, J. Chem. Phys. **49**, 5381 (1968).
[64]J. Heyd, G. E. Scuseria, and M. Ernzerhof, J. Chem. Phys. **118**, 8207 (2003).
[65]J. R. Reimers and R. O. Watts, Mol. Phys. **52**, 357 (1984).
[66]J. R. Reimers and R. O. Watts, Chem. Phys. **91**, 201 (1984).
[67]F. Santoro, R. Improta, A. Lami, J. Bloino, and V. Barone, J. Chem. Phys. **126**, 084509 (2007).
[68]L. Fiedor, M. Stasiek, B. Myśliwa-Kurdziel, and K. Strzałka, Photosynth. Res. **78**, 47 (2003).
[69]L. Fiedor, A. Kania, B. Myśliwa-Kurdziel, Ł. Orzeł, and G. Stochel, Biochim. Biophys. Acta, Bioenerg. **1777**, 1491 (2008).
[70]D. M. Palm, A. Agostini, A.-C. Pohland, M. Werwie, E. Jaenicke, and H. Paulsen, ACS Omega **4**, 7971 (2019).
[71]N. Verdal, P. M. Kozlowski, and B. S. Hudson, J. Phys. Chem. A **109**, 5724 (2005).
[72]A. G. Ozkabak, L. Goodman, and K. B. Wiberg, J. Chem. Phys. **92**, 4115 (1990).
[73]J. R. Reimers, L. McKemmish, R. H. McKenzie, and N. S. Hush, Phys. Chem. Chem. Phys. **17**, 24598 (2015).